

Exclusive Leptoproduction of ρ^0 Mesons from Hydrogen at Intermediate Virtual Photon Energies

The HERMES Collaboration

A. Airapetian³⁰, N. Akopov³⁰, I. Akushevich⁷, M. Amarian^{23,25,30}, J. Arrington², E.C. Aschenauer^{7,13,23}, H. Avakian^{11,a}, R. Avakian³⁰, A. Avetissian³⁰, E. Avetissian³⁰, P. Bailey¹⁵, B. Bains¹⁵, C. Baumgarten²¹, M. Beckmann¹², S. Belostotski²⁴, S. Bernreuther⁹, N. Bianchi¹¹, H. Böttcher⁷, A. Borissov^{6,14,19}, M. Bouwuis¹⁵, J. Brack⁵, S. Brauksiepe¹², B. Braun^{9,21}, W. Brückner¹⁴, A. Brüll^{14,18}, P. Budz⁹, H.J. Bulten^{17,23,29}, G.P. Capitani¹¹, P. Carter⁴, P. Chumney²², E. Cisbani²⁵, G.R. Court¹⁶, P.F. Dalpiaz¹⁰, R. De Leo³, L. De Nardo¹, E. De Sanctis¹¹, D. De Schepper^{2,18}, E. Devitsin²⁰, P.K.A. de Witt Huberts²³, P. Di Nezza¹¹, V. Djordjadze⁷, M. Düren⁹, A. Dvoredsky⁴, G. Elbakian³⁰, J. Ely⁵, A. Fantoni¹¹, A. Fechtchenko⁸, M. Ferro-Luzzi²³, K. Fiedler⁹, B.W. Filippone⁴, H. Fischer¹², B. Fox⁵, J. Franz¹², S. Frullani²⁵, Y. Gärber⁷, F. Garibaldi²⁵, E. Garutti^{10,23}, G. Gavrilov²⁴, V. Gharibyan³⁰, A. Golendukhin^{6,21,30}, G. Graw²¹, O. Grebeniuk²⁴, P.W. Green^{1,27}, L.G. Greeniaus^{1,27}, A. Gute⁹, W. Haeberli¹⁷, M. Hartig²⁷, D. Hasch^{7,11}, D. Heesbeen²³, F.H. Heinsius¹², M. Henoch⁹, R. Hertenberger²¹, W.H.A. Hesselink^{23,29}, P. Hoffmann-Rothe²³, G. Hofman⁵, Y. Holler⁶, R.J. Holt¹⁵, B. Hommez¹³, W. Hoprich¹⁴, G. Iarygin⁸, H. Ihssen^{6,23}, M. Iodice²⁵, A. Izotov²⁴, H.E. Jackson², A. Jgoun²⁴, R. Kaiser^{7,26,27}, J. Kanesaka²⁸, E. Kinney⁵, A. Kisselev²⁴, P. Kitching¹, H. Kobayashi²⁸, N. Koch⁹, K. Königsmann¹², M. Kolstein²³, H. Kolster^{21,23}, V. Korotkov⁷, E. Kotik¹, V. Kozlov²⁰, V.G. Krivokhijine⁸, G. Kyle²², L. Lagamba³, A. Laziev^{23,29}, P. Lenisa¹⁰, T. Lindemann⁶, W. Lorenzon¹⁹, N.C.R. Makins^{2,15}, J.W. Martin¹⁸, H. Marukyan³⁰, F. Masoli¹⁰, M. McAndrew¹⁶, K. McIlhany^{4,18}, R.D. McKeown⁴, F. Meissner⁷, F. Menden^{12,27}, A. Metz²¹, N. Meyners⁶, O. Mikloukho²⁴, C.A. Miller^{1,27}, R. Milner¹⁸, V. Mitsyn⁸, V. Muccifora¹¹, R. Mussa¹⁰, A. Nagaitsev⁸, E. Nappi³, Y. Naryshkin²⁴, A. Nass⁹, W.-D. Nowak⁷, T.G. O'Neill², R. Openshaw²⁷, J. Ouyang²⁷, B.R. Owen¹⁵, S.F. Pate^{18,22,b}, S. Potashov²⁰, D.H. Potterveld², G. Rakness⁵, R. Redwine¹⁸, D. Reggiani¹⁰, A.R. Reolon¹¹, R. Ristinen⁵, K. Rith⁹, D. Robinson¹⁵, M. Ruh¹², D. Ryckbosch¹³, Y. Sakemi²⁸, I. Savin⁸, C. Scarlett¹⁹, C. Schill¹², F. Schmidt⁹, M. Schmitt⁹, G. Schnell²², K.P. Schüller⁶, A. Schwind⁷, J. Seibert¹², T.-A. Shibata²⁸, T. Shin, V. Shutov⁸, C. Simani^{10,23,29}, A. Simon^{12,22}, K. Sinram⁶, E. Steffens⁹, J.J.M. Steijger²³, J. Stewart^{16,27}, U. Stösslein⁷, K. Suetsugu²⁸, M. Sutter¹⁸, H. Tallini, S. Taroian³⁰, A. Terkulov²⁰, S. Tessarin¹⁰, E. Thomas¹¹, B. Tipton^{18,4}, M. Tytgat¹³, G.M. Urciuoli²⁵, J.F.J. van den Brand^{23,29}, G. van der Steenhoven²³, R. van de Vyver¹³, J.J. van Hunen²³, M.C. Vetterli^{26,27}, V. Vikhrov²⁴, M.G. Vincter^{27,1}, J. Visser²³, E. Volk¹⁴, C. Weiskopf⁹, J. Wendland^{26,27}, J. Wilbert⁹, T. Wise¹⁷, K. Woller⁶, S. Yoneyama²⁸, H. Zohrabian³⁰,

¹Department of Physics, University of Alberta, Edmonton, Alberta T6G 2J1, Canada^c

²Physics Division, Argonne National Laboratory, Argonne, Illinois 60439-4843, USA^d

³Istituto Nazionale di Fisica Nucleare, Sezione di Bari, 70124 Bari, Italy

⁴W.K. Kellogg Radiation Laboratory, California Institute of Technology, Pasadena, California 91125, USA^e

⁵Nuclear Physics Laboratory, University of Colorado, Boulder, Colorado 80309-0446, USA^f

⁶DESY, Deutsches Elektronen Synchrotron, 22603 Hamburg, Germany

⁷DESY Zeuthen, 15738 Zeuthen, Germany

⁸Joint Institute for Nuclear Research, 141980 Dubna, Russia

⁹Physikalisches Institut, Universität Erlangen-Nürnberg, 91058 Erlangen, Germany^{g,h}

¹⁰Istituto Nazionale di Fisica Nucleare, Sezione di Ferrara and Dipartimento di Fisica, Università di Ferrara, 44100 Ferrara, Italy

¹¹Istituto Nazionale di Fisica Nucleare, Laboratori Nazionali di Frascati, 00044 Frascati, Italy

¹²Fakultät für Physik, Universität Freiburg, 79104 Freiburg, Germany^g

¹³Department of Subatomic and Radiation Physics, University of Gent, 9000 Gent, Belgiumⁱ

¹⁴Max-Planck-Institut für Kernphysik, 69029 Heidelberg, Germany

¹⁵Department of Physics, University of Illinois, Urbana, Illinois 61801, USA^j

¹⁶Physics Department, University of Liverpool, Liverpool L69 7ZE, United Kingdom^k

¹⁷Department of Physics, University of Wisconsin-Madison, Madison, Wisconsin 53706, USA^l

¹⁸Laboratory for Nuclear Science, Massachusetts Institute of Technology, Cambridge, Massachusetts 02139, USA^m

¹⁹Randall Laboratory of Physics, University of Michigan, Ann Arbor, Michigan 48109-1120, USAⁿ

²⁰Lebedev Physical Institute, 117924 Moscow, Russia

²¹Sektion Physik, Universität München, 85748 Garching, Germany^g

²²Department of Physics, New Mexico State University, Las Cruces, New Mexico 88003, USA^o

²³Nationaal Instituut voor Kernfysica en Hoge-Energiefysica (NIKHEF), 1009 DB Amsterdam, The Netherlands^p

²⁴Petersburg Nuclear Physics Institute, St. Petersburg, Gatchina, 188350 Russia

²⁵Istituto Nazionale di Fisica Nucleare, Sezione Sanità and Physics Laboratory, Istituto Superiore di Sanità, 00161 Roma, Italy

²⁶Department of Physics, Simon Fraser University, Burnaby, British Columbia V5A 1S6, Canada^c

²⁷TRIUMF, Vancouver, British Columbia V6T 2A3, Canada^c

²⁸Department of Physics, Tokyo Institute of Technology, Tokyo 152, Japan^g

²⁹Department of Physics and Astronomy, Vrije Universiteit, 1081 HV Amsterdam, The Netherlands^p

³⁰Yerevan Physics Institute, 375036, Yerevan, Armenia

^a supported by INTAS contract No. 93-1827

^b partially supported by the Thomas Jefferson National Accelerator Facility, under DOE contract DE-AC05-84ER40150.

^c supported by the Natural Sciences and Engineering Research Council of Canada (NSERC)

^d supported by the US Department of Energy, Nuclear Physics Div., grant No. W-31-109-ENG-38

^e supported by the US National Science Foundation, grant No. PHY-9420470

^f supported by the US Department of Energy, Nuclear Physics Div., grant No. DE-FG03-95ER40913

^g supported by the Deutsche Bundesministerium für Bildung, Wissenschaft, Forschung und Technologie

^h supported by the Deutsche Forschungsgemeinschaft

ⁱ supported by the FWO-Flanders, Belgium

^j supported by the US National Science Foundation, grant No. PHY-9420787

^k supported by the U.K. Particle Physics and Astronomy Research Council

^l supported by the US Department of Energy, Nuclear Physics Div., grant No. DE-FG02-88ER40438, and the US National Science Foundation, grant No. PHY-9722556

^m supported by the US Department of Energy, Nuclear Physics Div.

ⁿ supported by the US National Science Foundation, grant No. PHY-9724838

^o supported by the US Department of Energy, Nuclear Physics Div., grant No. DE-FG03-94ER40847

^p supported by the Dutch Foundation for Fundamenteel Onderzoek der Materie (FOM)

^q supported by Monbusho, JSPS and Toray Science Foundation of Japan

Received: April 25, 2000; Revised: July 3, 2000

Abstract. Measurements of the cross section for exclusive virtual-photoproduction of ρ^0 mesons from hydrogen are reported. The data were collected by the HERMES experiment using 27.5 GeV positrons incident on a hydrogen gas target in the HERA storage ring. The invariant mass W of the photon-nucleon system ranges from 4.0 to 6.0 GeV, while the negative squared four-momentum Q^2 of the virtual photon varies from 0.7 to 5.0 GeV². The present data together with most of the previous data in the intermediate W -domain are well described by a model that infers the W -dependence of the cross section from the dependence on the Bjorken scaling variable x of the unpolarized structure function for deep-inelastic scattering. In addition, a model calculation based on Off-Forward Parton Distributions gives a fairly good account of the longitudinal component of the ρ^0 production cross section for $Q^2 > 2$ GeV².

1 Introduction

This paper presents cross section measurements for exclusive diffractive production of $\rho^0(770)$ vector mesons in positron scattering on a ^1H target. The production of vector mesons by real or virtual photons is of considerable interest, as the corresponding cross section is closely related to other observables in lepton scattering. For example, with help of the recently introduced Off-Forward Parton Distributions (OFPDs), one can relate elastic nucleon form factors, deep-inelastic scattering (DIS) structure functions, virtual Compton scattering cross sections, and vector meson production cross sections [1–8]. The OFPDs represent a generalization of the parton distributions measured, for instance, in inclusive DIS experiments.

In Refs. [5, 6] the longitudinal part of the ρ^0 virtual-photon production cross section is calculated in the OFPD framework. At large values of the photon-nucleon invariant mass ($W > 10$ GeV) the calculated cross section is

dominated by a two-gluon exchange mechanism, which has been treated using the perturbative approach of Ref. [4]. These calculations reproduce existing data. However, uncertainties arise due to the size of higher-order and higher-twist contributions [4, 7–9], which are larger at small values of Q^2 (the negative square of the four-momentum of the virtual photon). Below 10 GeV the calculated cross section is dominated (in leading twist) by a handbag diagram, in which the virtual photon is absorbed by a valence quark in the nucleon [5, 6]. Following Ref. [5] this mechanism is called quark exchange. However, few data are available between 4 and 10 GeV. Several data sets exist for $W < 4$ GeV, but in this domain the OFPD calculations do not apply, as the reaction receives contributions from other reaction channels in this domain.

The relation between the vector meson lepton production cross section and the structure function $F_2^{\text{D}}(x)$ of the proton (with x the Bjorken scaling variable) is apparent

in a model calculation by Haakman et al. [10] based on Reggeon field theory. In this model the x -dependence of $F_2^p(x)$ is related to the W -dependence of the cross section for vector meson leptonproduction. The model gives a good description of $\gamma^*p \rightarrow \rho^0p$ cross sections for W ranging from 10 to 180 GeV. Between 4 and 10 GeV the calculated shape of the W -dependence changes significantly with Q^2 . The model has not yet been properly assessed in this domain due to lack of data.

The two examples above illustrate the need for additional exclusive ρ^0 leptonproduction data in the W -range between 4 and 10 GeV. Such data are reported in the present paper. Exclusive cross sections have been measured for W values between 4.0 and 6.0 GeV, and Q^2 values between 0.7 and 5.0 GeV². The kinematical variables used to describe ρ^0 leptonproduction are introduced in the next section. Experimental details are provided in section 3, while the data analysis is discussed in section 4. The experimental results are compared to various model calculations in section 5, and the paper is summarized in the last section.

2 Kinematics

In the present leptonproduction measurement both the scattered lepton and two oppositely charged hadrons are observed. The ρ^0 leptonproduction events are identified by requiring that the reconstructed invariant mass of the two hadrons is close to the mass of the ρ^0 meson, i.e. 0.77 GeV. The kinematic variables that characterize such measurements are defined here in the laboratory frame. The variables describing the kinematics of the virtual photon include its energy ν , its fractional energy $y = \nu/E_0$ (with E_0 the incident lepton energy), and its four-momentum q . The latter quantity is related to the previously introduced variable Q^2 through $Q^2 = -q^2 > 0$. The Bjorken scaling variable x is related to ν and Q^2 by $x = Q^2/(2M\nu)$, and the photon-nucleon invariant mass W is given by $W^2 = M^2 + 2M\nu - Q^2$. The virtual-photon polarization parameter is represented by ϵ .

The ρ^0 meson is characterized by its four-momentum v and $\theta_{\pi\pi}$, which represents the angle between the two pions into which the ρ^0 meson decays.

Combining some of the lepton and meson variables, one can introduce $t = (q - v)^2 < 0$, the square of the four-momentum exchange between the virtual photon and the target, and $\Delta E = (P_Y^2 - M^2)/2M$, which is a measure of the missing energy (where $P_Y = P + q - v$ represents the 4-momentum of the unobserved final state Y with $P = (M, 0)$ that of the target nucleon).

Instead of $-t$, the above-threshold momentum transfer $-t' = -t + t_0$ is often used, which is approximately equal to p_t^2 – the square of the transverse momentum of the ρ^0 meson with respect to the direction \mathbf{q} . In this expression $-t_0$ represents the minimum value of $-t$ for fixed values of ν , Q^2 and P_Y^2 .

3 Experiment

The data were collected during the 1996 and 1997 running periods of the HERMES experiment [11] at DESY using a 27.5 GeV longitudinally polarized positron beam with a ¹H gas target in the HERA storage ring. Part of the data set was collected with longitudinally polarized targets. Since the polarization degrees of freedom were not exploited in the present analysis, the average over both target polarization states is taken.

The HERMES polarized proton target [12] is formed by injecting a nuclear-polarized beam of atomic hydrogen from an atomic beam source into a tubular open-ended storage cell inside the positron ring. The cell provides a 40 cm long target of pure atomic species with an areal density of approximately 7×10^{13} atoms/cm². With unpolarized targets of molecular hydrogen, areal densities of about 10^{15} atoms/cm² were obtained. The storage cell was shielded from synchrotron radiation by two sets of collimators, one of which is moveable. No particles were observed to originate from scattering events in the walls of the storage cell.

During the course of one fill (typically 8 hours long), the positron current in the ring decreased from typically 30 – 40 mA at injection to ~ 10 mA, at which point the ring was emptied. The data presented in this paper correspond to an integrated luminosity of 108 pb^{-1} .

The HERMES spectrometer is described in detail elsewhere [11]. It is a forward spectrometer in which both the scattered positron and produced hadrons are detected within an angular acceptance ± 170 mrad horizontally, and $\pm (40 - 140)$ mrad vertically. The scattered-positron trigger was formed from a coincidence between a pair of scintillator hodoscope planes and a lead-glass calorimeter. The trigger required an energy of more than 3.5 GeV deposited in the calorimeter. (For part of the running the trigger threshold was reduced to 1.5 GeV, for which a correction was applied in the data analysis.) Positron identification was accomplished using the calorimeter, the preshower counter consisting of the second hodoscope preceded by a lead sheet, a transition-radiation detector, and a threshold gas Čerenkov counter. This system provided positron identification with an average efficiency of 99% and a hadron contamination of less than 1%.

4 Data analysis

Only those events were selected that contained a scattered positron and exactly two hadrons with opposite charge. (A more detailed description of the analysis is given in Refs. [13, 14].) A number of geometric requirements were imposed on the particle tracks to ensure that they were well contained within the acceptance of the spectrometer. It was also required that the tracks originated from along the beam line within ± 18 cm of the centre of the target. In addition, several constraints were imposed on the kinematic variables. The size of the radiative corrections was limited by requiring $y \leq 0.85$. Because the W -acceptance

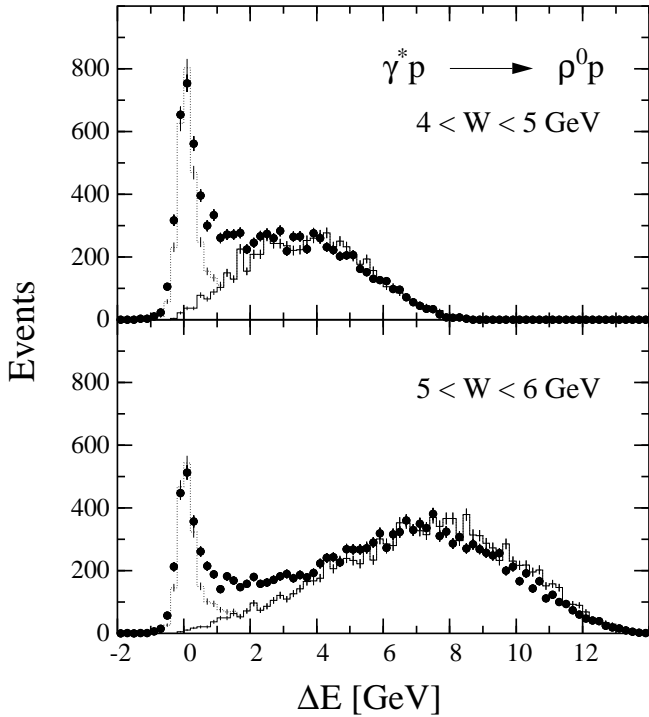


Fig. 1. Missing energy spectra for lepton production of ρ^0 mesons off ^1H at an incident energy of 27.5 GeV. The upper (lower) panel corresponds to the W -range between 4 and 5 (5 and 6) GeV. The data have been selected requiring $0.6 \text{ GeV} < M_{\pi\pi} < 1 \text{ GeV}$ and $-t' < 0.4 \text{ GeV}^2$. The solid histograms represent the results of a Monte Carlo simulation [15] of the background, which has been scaled to the data for $\Delta E > 3.0 \text{ GeV}$. The dotted histogram includes a simulation [14] of exclusive ρ^0 -production as well. As the Monte Carlo simulations do not include inelastic nucleon excitations or internal radiative effects for the exclusive channel, the ΔE -region between 0.5 and 2.5 GeV cannot be properly described.

of the HERMES spectrometer for ρ^0 production is sharply reduced both below 4 GeV and above 6 GeV, cross sections for only two W -bins (4–5 and 5–6 GeV) have been extracted from the data.

The ρ^0 vector mesons were identified by requiring $0.6 \text{ GeV} < M_{\pi\pi} < 1 \text{ GeV}$, with $M_{\pi\pi}$ the invariant mass of the pair of detected hadrons, assuming that they are pions. It has been verified that this requirement also removes the $\phi \rightarrow \text{K}^+\text{K}^-$ background, by confirming that the ϕ events, which occur at $M_{\text{KK}} \approx M_\phi$, appear in the $M_{\pi\pi}$ spectrum at $M_{\pi\pi} < 0.6 \text{ GeV}$. Here M_{KK} is the invariant mass calculated assuming that the two hadrons are kaons, and $M_\phi = 1.019 \text{ GeV}$ is the mass of the ϕ meson.

In exclusive ρ^0 electroproduction, i.e. $eN \rightarrow e'\rho^0N$, the part of the final state that is unobserved at HERMES consists of a nucleon recoiling without excitation. Such events are selected by requiring that the missing energy ΔE is approximately zero. In this domain the ΔE spectrum, as displayed in Fig. 1 for the two W -bins, shows a clear peak near $\Delta E \approx 0$. The exclusive events were selected by requiring $\Delta E < 0.4 \text{ GeV}$.

Using the Monte Carlo simulation for exclusive ρ^0 production described in section 4.2, it has been evaluated that on average 18% of the exclusive events fall outside the imposed ΔE window. This effect has been accounted for (bin by bin) in the acceptance correction.

The requirement on ΔE is relatively tight in order to suppress inelastic contributions involving nucleon excitations. As no Monte Carlo simulation is available for such double diffractive processes, their remaining contribution is estimated from other data in section 4.3.

4.1 Background subtraction

There is a background contribution under the exclusive ρ^0 peak that is caused by hadrons from DIS fragmentation processes. Part of this background is removed by excluding the region $-t' > 0.4 \text{ GeV}^2$, where the background dominates the ρ^0 yield. The remaining background is estimated and subtracted using the methods described below.

The background estimate is based on the LEPTO Monte Carlo program [15]. This simulation includes hadrons resulting from fragmentation processes in deep-inelastic scattering (using the Lund fragmentation code), but not from diffractive ρ^0 production. The ΔE spectrum was generated independently for each (Q^2, W) -bin, and normalized to the experimental data in the ΔE region above 3.0 GeV (see Fig. 1). Thus normalized, the background was subtracted from the data in the ΔE domain that was used for the determination of the cross section. Depending on kinematics the background contribution ranges from $(3 \pm 1)\%$ to $(9 \pm 4)\%$, where the uncertainties include the effect of varying the ΔE -ranges used in evaluating the background contribution. The lower limit of the ΔE -range used to normalize the background was varied from 3 to 5 GeV, and the upper limit used in selecting the exclusive events was varied from 0.3 to 0.6 GeV.

The background subtraction procedure was verified by also using an alternative method. In this case a ΔE spectrum was extracted from the data by requiring $-t'$ values between 0.7 and 5 GeV^2 , i.e. well beyond the region used to determine the diffractive cross section. A similar normalization procedure is used, i.e. the background spectrum is normalized such as to reproduce the same number of events for $\Delta E > 3 \text{ GeV}$ as in the spectrum obtained with the standard $-t'$ requirement. The tail of the normalized background spectrum for $\Delta E < 0.4 \text{ GeV}$ was taken to represent the actual background contribution to the ρ^0 mass peak. The cross sections obtained after this background subtraction method were found to be consistent with those obtained using the Monte-Carlo based method within the systematic errors listed below in Table 1.

4.2 Acceptance correction

The data were corrected for the finite acceptance and inefficiencies of the HERMES spectrometer for ρ^0 production. The correction was evaluated using a Monte Carlo simulation based on the Vector Meson Dominance (VMD)

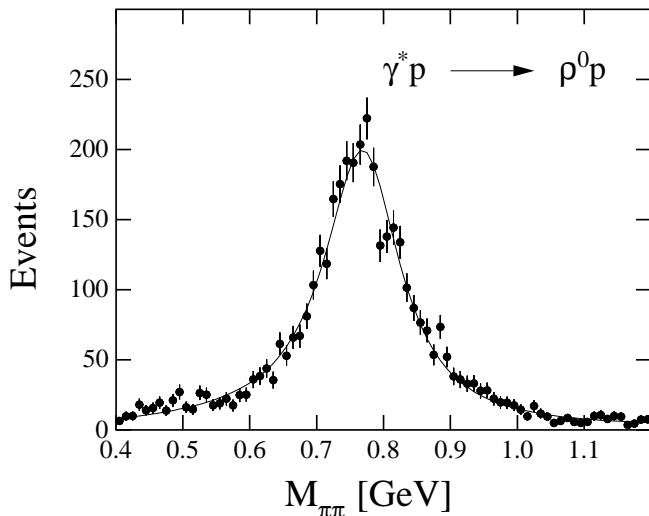


Fig. 2. Invariant mass spectrum of the two oppositely charged hadrons assuming that they are pions. Backgrounds have been subtracted, the contribution from ϕ decays has been removed by requiring that $M_{KK} > 1.04$ GeV, and the acceptance correction has been applied. The ρ^0 mass peak at 770 MeV is described by a Breit-Wigner function (solid line), of which the parameters were fitted to the data.

model. Details are given in Ref. [14]. For each kinematic variable (ν , Q^2 , W , $M_{\pi\pi}$, $\cos\theta_{\pi\pi}$ and $-t'$) good agreement between the measured distribution and the simulation was obtained.

The acceptance correction is large because the HERMES spectrometer has a relatively small acceptance for $\gamma^*p \rightarrow \rho^0p$ events. The acceptance for ρ^0 mesons (given an observed scattered positron) ranges from only 5.9% at low Q^2 to 18% at high Q^2 . As the corresponding correction factors are large, it is mandatory to study the dependence of the acceptance correction on the details of the Monte Carlo calculation. For that purpose, the entire analysis was redone varying the assumptions for the angular distributions of the production and decay of the ρ^0 -meson. The original Monte Carlo simulation, which assumed s-Channel Helicity Conservation (SCHC), was replaced by one that produces uniform angular distributions for all relevant angles. In addition, the Q^2 -dependence of the VMD propagator (as given by Eq. 2 in section 5.1) was varied by changing the exponent from 2 to 2.5, and an alternative event generator DIPSI [16] was used. The sensitivity of the Monte Carlo yield to variations of the angular distributions and changes of the assumed Q^2 -dependence leads to typical systematic uncertainties of 10% and 6%, respectively. The effect of the event generator itself amounts to typically 8%. Including all variations, the uncertainty of the cross sections due to the acceptance correction ranges from 12% to 17%, depending on the kinematics.

4.3 Cross section determination

The $M_{\pi\pi}$ mass spectrum is shown in Fig. 2. In this spectrum backgrounds are subtracted, the acceptance correc-

tion is applied and all kinematic requirements mentioned above are imposed. The ρ^0 mass peak was fitted using a Breit-Wigner (p-wave) function and a constant background term representing the non-resonant physics background. The Breit-Wigner function was multiplied by the factor $(M_\rho/M_{\pi\pi})^{n_s}$ in which n_s represents the skewing parameter. This procedure is identical to the one described in Ref. [17], and was first proposed by Ross and Stodolsky [18]. The resulting fit parameters ($M_{\rho^0} = 0.776 \pm 0.003$ GeV, $\Gamma_{\rho^0} = 0.147 \pm 0.009$ GeV, and $n_s = 2.2 \pm 0.4$) are in good agreement with the values published by E665 [17]: $M_{\rho^0} = 0.777 \pm 0.002$ GeV, $\Gamma_{\rho^0} = 0.146 \pm 0.003$ GeV, and $n_s = 2.7 \pm 0.6$ (for the same Q^2 -region). Both experiments find a background term that is consistent with zero, and are in fair agreement with the PDG-values [19]: $M_{\rho^0} = 0.7700 \pm 0.0008$ GeV, $\Gamma_{\rho^0} = 0.1507 \pm 0.0011$ GeV. If the effect of the ω decay is also considered in the fit, ω mass and width parameters are found that are also consistent with Ref. [19]. The contribution of this interference averages out to zero in the considered mass interval. The absolute contribution of ω -production to the apparent ρ^0 yield is estimated to be less than 1%, and has therefore been neglected. It should be noted that the ρ^0 production cross sections presented in this paper correspond to the data in the mass region $0.6 \text{ GeV} < M_{\pi\pi} < 1.0 \text{ GeV}$ with a correction (of $14 \pm 2\%$) for the tails of the skewed Breit-Wigner distribution [18] outside this mass window. This correction factor has been evaluated relative to the mass range between $2M_\pi$ and $(M_{\rho^0} + 5\Gamma_{\rho^0})$.

Examples of the $-t'$ distribution of the data can be found in Refs. [14,20]. The $-t'$ distribution is fit to a falling exponential, and the fit is used to correct the measured cross section for the excluded region $-t' > 0.4 \text{ GeV}^2$. The slope parameter b from the fit is $(6.82 \pm 0.15) \text{ GeV}^{-2}$, which is consistent with previously published values.

The ρ^0 production data were normalized using the inclusive deep-inelastic scattering (DIS) yield derived from the same data sample. By comparing the DIS yield to the LEPTO Monte-Carlo yield based on the world data [21] evaluated at the appropriate Q^2 and x values, the required normalization factors were determined. Virtual photoproduction cross sections, $\sigma_{\gamma^*p \rightarrow \rho^0p}$, were obtained from the leptoproduction cross section after applying the photon flux factor Γ_T (using the Hand convention as outlined in Ref. [17], for instance):

$$\sigma_{\gamma^*p \rightarrow \rho^0p} = \frac{1}{\Gamma_T} \frac{d\sigma_{ep \rightarrow e'\rho^0p}}{d\nu dQ^2} \quad (1)$$

In double-diffractive (DD) processes the target nucleon is broken up. In a recent study of target dissociation in ρ^0 production at center-of-mass energies between 60 and 180 GeV, the cross section ratio of double-diffractive to single-diffractive ρ^0 production was measured to be 0.65 ± 0.17 [22]. Accounting for the shape of the baryonic spectrum (taken from pp diffractive scattering [23]) and the resolution of the present experiment, the DD contribution to the diffractive ρ^0 production cross section at HERMES is found to be $(4 \pm 2)\%$, for which the data were corrected. The uncertainty in the DD contribution origi-

Table 1. The measured virtual-photoproduction cross sections $\sigma_{\gamma^* p \rightarrow \rho^0 p}$ for exclusive ρ^0 production on ^1H (in μb) corrected for radiative effects. Both the statistical (first) and systematic (second) uncertainties are listed.

$\langle Q^2 \rangle$ [GeV^2]	$\langle W \rangle = 4.6$ GeV	$\langle W \rangle = 5.4$ GeV
0.83	$2.46 \pm 0.13 \pm 0.51$	$2.04 \pm 0.10 \pm 0.43$
1.3	$0.92 \pm 0.03 \pm 0.15$	$1.00 \pm 0.04 \pm 0.16$
2.3	$0.43 \pm 0.02 \pm 0.08$	$0.41 \pm 0.02 \pm 0.07$
4.0	$0.16 \pm 0.01 \pm 0.03$	$0.10 \pm 0.01 \pm 0.02$

nates from a rough estimate of the acceptance for double diffractive events relative to that for single diffractive ρ^0 events, and the uncertainty of the data of Ref. [22]. Taking into account other estimates of the ratio of double diffractive to single diffractive ρ^0 production also at lower W -values [24], which are smaller in general, a total systematic uncertainty of about 3% (relative to the measured cross section) has been assigned to the DD contribution. The small size of the DD contribution is related to the good energy resolution of the HERMES experiment ($\sigma_{\Delta E} \approx 0.25$ GeV – see Fig. 1).

The final cross sections are obtained by applying a radiative correction to the experimentally determined ρ^0 production cross section. The internal radiative correction has been evaluated separately for each (Q^2, W) bin, and typically amounts to 18% [25]. External radiative effects (caused by detector materials) are included in the acceptance Monte Carlo.

5 Results

In Table 1 the results for the ρ^0 virtual-photoproduction cross section are given for each Q^2 and W bin. The systematic uncertainties are dominated by those from the acceptance correction factors, which amount to 17%, 11%, 14% and 17% in the bins centered at Q^2 values of 0.83, 1.3, 2.3 and 4.0 GeV^2 , respectively. Another important contribution to the systematic uncertainty stems from the uncertainty in the reconstruction and data selection efficiency, which totals about 9%. This contribution has been estimated by varying the large number of requirements used to select data and reconstruct valid events. The quoted 9% also includes uncertainties in tracking efficiency, kaon contamination, radiative corrections and DD-contribution. Remaining contributions to the total systematic uncertainty are the absolute normalization (6%) and the background subtraction (4%). The combined systematic uncertainty on the ρ^0 cross sections ranges from 16 to 21%, depending on the kinematics.

In Fig. 3 the virtual-photoproduction cross section is plotted versus W , and compared to existing measurements [17, 26–30] at nearby values of W . As the various data sets have been measured at different average Q^2 values, most data sets were rescaled to the average Q^2 values of the HERMES data using the Q^2 -dependence of the VMD model, which is in agreement with the present data as will be shown below (see Fig. 4 and Eq. (2) with $m =$

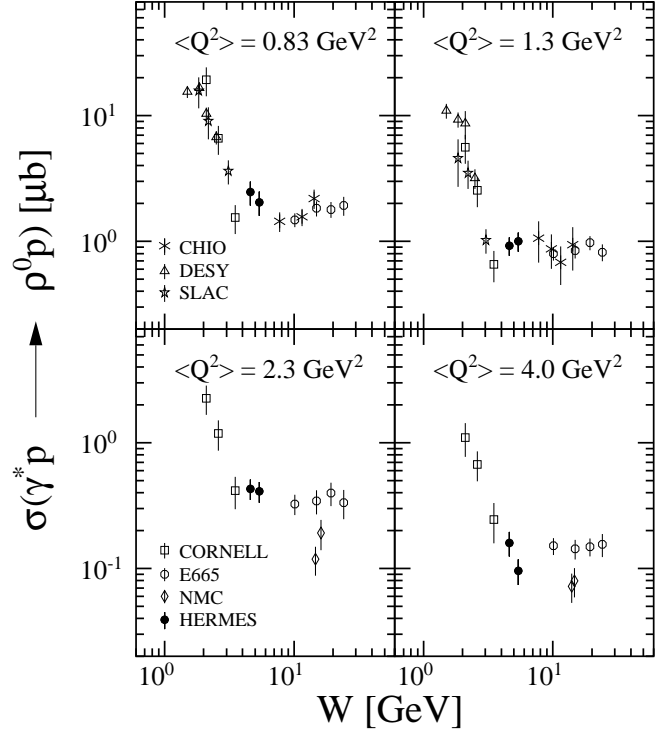


Fig. 3. The virtual-photoproduction cross section for exclusive ρ^0 production versus W for the indicated values of $\langle Q^2 \rangle$. The data collected in the present experiment are represented by solid circles. The open squares are from Ref. [28], the open triangles from Ref. [26], the open stars from Ref. [27], the crosses from Ref. [29], the open circles from Ref. [17], and the open diamonds from Ref. [30]. Previous data have been scaled to the presently used Q^2 -bins using Eq. (2). The error bars include both the statistical and systematic uncertainties (added in quadrature).

2). It is noted that the various data sets have also been obtained at different average ϵ -values, for which no correction has been applied. The HERMES data are seen to fill the gap which previously existed between the steeply declining data at low W , and the data collected at higher W values, which have a much flatter W -dependence. With a few exceptions, there is a fair consistency among the world's data on exclusive ρ^0 production. The first exception concerns the highest W point (at 3.5 GeV) of the Cornell data [28] at $Q^2 = 0.83$ GeV^2 , which deviates by about 2σ – 3σ from a smooth interpolation of all other data in that W -region. Secondly, there is a difference of about a factor of two between the NMC [30] and E665 data [17] at $W \approx 15$ GeV in the two highest Q^2 -bins. The latter discrepancy has been reported before [17, 31]. Part of the discrepancy might be related to a (model-dependent) subtraction of the non-resonant contribution to the ρ^0 -peak that was applied by NMC [30] in contrast to E665 [17] and the present experiment.

It should be noted that it is the total cross section for the process $ep \rightarrow eh^+h^-p$ with $M_{\pi\pi} \approx M_{\rho^0}$ that is displayed in fig. 3 for all data sets. This total cross section is believed to receive contributions from exclusive ρ^0

Table 2. The fitted photoproduction cross sections for ρ^0 production on ^1H . In the top row the results are shown with the variables σ_0 and ξ^2 of Eq. (2) as free parameters, the middle row lists the results obtained with σ_0 and m left free, and the bottom row shows the fitted values of m if a parameterization of the world data is used to constrain σ_0 . The listed errors include both the statistical and systematic uncertainties, added in quadrature. In all cases the $\chi^2/\text{d.o.f.}$ values of the fits are close to or less than unity.

Variables	$\langle W \rangle = 4.6 \text{ GeV}$	$\langle W \rangle = 5.4 \text{ GeV}$
σ_0 [μb]	10.7 ± 1.8	13.1 ± 1.7
ξ^2	-0.023 ± 0.049	-0.13 ± 0.03
σ_0 [μb]	11.2 ± 2.9	19.7 ± 4.9
m	2.42 ± 0.18	2.83 ± 0.18
σ_0 [μb]	11.5 (fixed)	11.0 (fixed)
m	2.44 ± 0.05	2.46 ± 0.06

production through Reggeon exchange, as well as from reaction channels such as those involving nucleon resonances at low W , as reported in Refs. [26–28]. In virtual-photoproduction it is usually assumed that the latter contributions are negligible beyond $W \approx 4 \text{ GeV}$. The data of Fig. 3 indicate that these additional processes have a decreasing contribution to ρ^0 production up to about 4–5 GeV, where the steep decrease of the cross section changes into an almost flat W -dependence. Henceforth, we restrict the comparison with existing calculations to data collected at $W > 4 \text{ GeV}$.

5.1 Q^2 -dependence

The HERMES data are displayed in Fig. 4 as a function of Q^2 for the two W bins. For the purpose of extrapolating to $Q^2 = 0$, the Q^2 -dependence of the data has been parameterized using the following functional form, inspired by the VMD model [17, 32]

$$\sigma(Q^2) = \sigma_0 \cdot \left(\frac{M_\rho^2}{Q^2 + M_\rho^2} \right)^m \cdot (1 + \epsilon R(Q^2)). \quad (2)$$

The VMD-model predicts that $m = 2$ and that the ratio of longitudinal to transverse ρ^0 photoproduction cross sections is given by $R = \xi^2 Q^2 / M_\rho^2$. A good description of the data is obtained by fixing m to its VMD value, and treating σ_0 and ξ^2 as free parameters. Here σ_0 represents the ρ^0 production cross section for real ($Q^2 = 0$) photons. The results of the fit (solid curves in Fig. 4) are listed in table 2.

As the ratio R must be positive, the negative fit values of ξ^2 indicate a deficiency of the VMD-model. Hence, a different approach was also used, i.e. the exponent m of the propagator in Eq. (2) was used as a free parameter, while the value of $R(Q^2)$ was fixed using information extracted from measurements of the ρ^0 decay angular distribution [14]:

$$R(W, Q^2) = c_0(W) \cdot (Q^2 / M_\rho^2)^{c_1}. \quad (3)$$

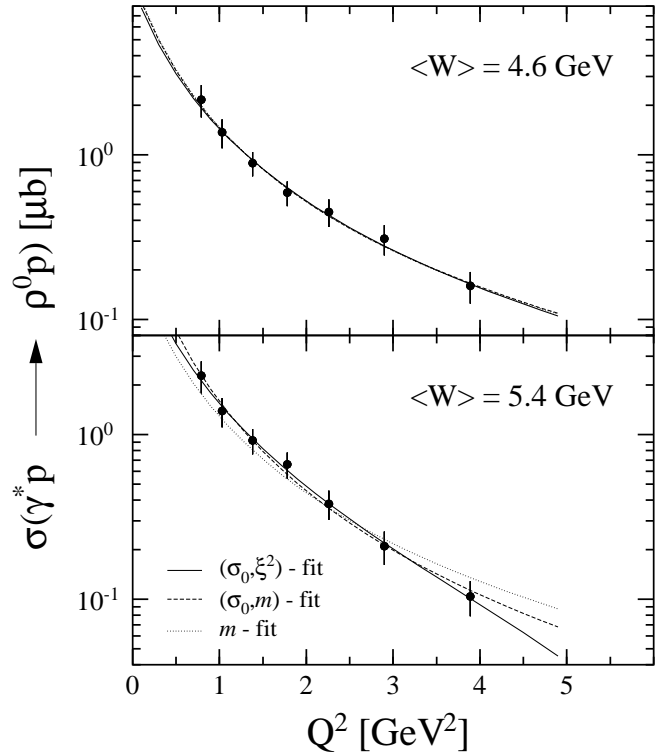


Fig. 4. The virtual-photoproduction cross section for ρ^0 production on ^1H versus Q^2 for $4 \text{ GeV} < W < 5 \text{ GeV}$ (upper panel) and $5 \text{ GeV} < W < 6 \text{ GeV}$ (lower panel). The error bars include both the statistical and systematic uncertainties, added in quadrature. The solid, dashed and dotted curves represent fits using the values of σ_0 and ξ^2 , σ_0 and m , or only m as free parameters, respectively.

The parameterization of R expressed by Eq. (3) has been obtained from a fit of the world data on R , yielding $c_1 = 0.61 \pm 0.04$, and $c_0(W) = 0.33 \pm 0.03$ (0.48 ± 0.03) for $4 \text{ GeV} < W < 7 \text{ GeV}$ ($W > 7 \text{ GeV}$). The resulting fits (dashed curves in Fig. 4) also give a good account of the Q^2 -dependence of the ρ^0 production cross section. The fitted parameters are listed in the middle row of table 2. The values of σ_0 are somewhat different from the results of the previous method, but are consistent as the errors have increased considerably.

It is concluded that an increase of the exponent m can avoid the negative values of ξ^2 found in the previous fits. This result quantitatively confirms similar conclusions obtained by the E665 collaboration ($m = 2.51 \pm 0.07$ at $W \approx 15 \text{ GeV}$ [17]).

The fitted values of the extrapolated photoproduction cross section σ_0 are in agreement with existing real-photon data [33], but carry larger error bars particularly if the exponent and the cross section are treated as free parameters. Since the VMD cross section scales with Q^{-4} while a perturbative QCD description predicts [34] that the longitudinal part of the cross section scales with Q^{-6} , it is of particular interest to study the value of the exponent of the propagator in the transitional domain probed by the present data. By fixing the value of the photoproduc-

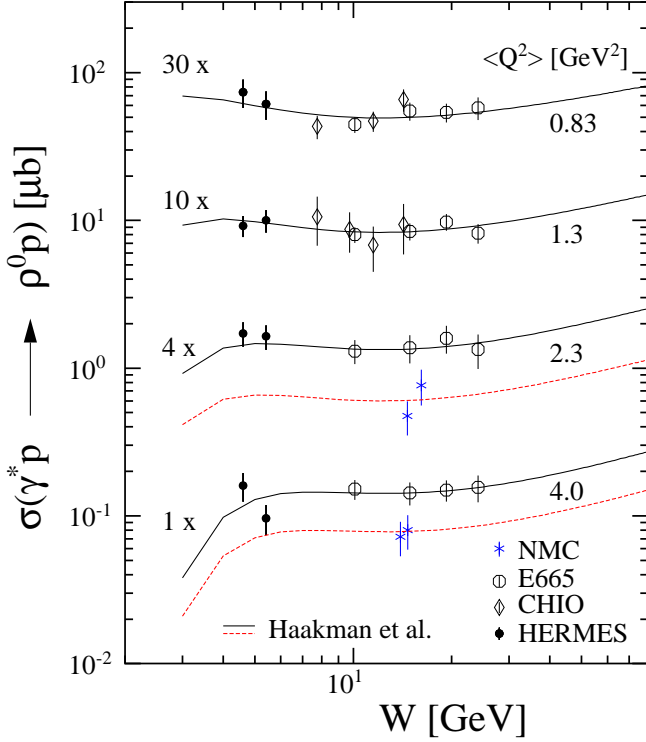


Fig. 5. The virtual-photoproduction cross section for ρ^0 production versus W at average Q^2 values of 0.83, 1.3, 2.3 and 4.0 GeV^2 (from top to bottom). The coding of the data symbols is the same as in Fig. 2. The solid (and dashed) lines represent the results of calculations by L. Haakman *et al.* [10]. For the solid (dashed) lines the HERMES and E665 (NMC) data were used to normalize the curves. Note that both the data and the calculations have been multiplied by the factors indicated on the left-hand side of the figure for plotting purposes only.

tion cross section σ_0 using a parameterization of the existing photoproduction data [33], a one-parameter fit of the Q^2 -dependence of the cross section has been carried out, yielding fairly precise values for the exponent m as can be seen from the bottom row of table 2. The fitted value is remarkably close to 2.5, which is in agreement with results obtained by E665 [17] (2.51 ± 0.07) at an average W value of 17 GeV, but somewhat above the result obtained by H1 [35] (2.24 ± 0.09) at $W = 75$ GeV.

5.2 W -dependence

In Fig. 5 the ρ^0 virtual-photoproduction cross sections are shown as a function of W for the four different Q^2 bins. As was argued above, only the data for $W > 4$ GeV are being considered. The data are compared to the calculations of Haakman *et al.* [10], which relate the W -dependence of the vector-meson production cross section to the proton structure function $F_2^p(x, Q^2)$. In order to understand how the x -dependence of $F_2^p(x, Q^2)$ influences the W -dependence of the ρ^0 production cross section, it is useful to realize that x and W are related by $W^2 = Q^2 \frac{1-x}{x} + M^2$, thus showing that the two variables are essentially inversely

proportional at large values of Q^2 and small values of x . The relation between the ρ^0 production cross section and the structure function is apparent in the expression for the t -dependence of the cross section given in Ref. [10]:

$$\frac{d\sigma}{dt} = f_\rho(Q^2) F_2^p(x, Q^2)^2 \exp[\Lambda(W)t]. \quad (4)$$

In this expression the scaling function $f_\rho(Q^2)$ is not determined by the model, and has been obtained from a fit to the experimental data displayed in Fig. 5. For $F_2^p(x, Q^2)$ the parameterization of Capella *et al.* [36] in terms of Pomeron and Reggeon exchanges has been taken. The slope parameter Λ is given by

$$\Lambda(W) = 2[R_{sc}^2 + 2\alpha'_P \ln(W/W_0)] \quad (5)$$

with the radius parameter $R_{sc}^2 = R_p^2 + R_V^2(Q^2)$ expressing the combined size of the scattering objects, and W_0^2 given by $M_{\rho^0}^2 + Q^2$. Expressions for α'_P , the slope of the effective Pomeron trajectory, and $R_V^2(Q^2)$ are given in Ref. [10]. Thus evaluated, the value of Λ turns out to be consistent with the value of the slope parameter derived from a fit of the $-t'$ distributions [10].

In order to compare the W -dependence of the model of Ref. [10] to that of the data, the calculations have been normalized to the HERMES and E665 data, for each Q^2 bin separately. The results are displayed in Fig. 5 for Q^2 bins centered at 0.83, 1.3, 2.3 and 4.0 GeV^2 , respectively. A good description of these data is obtained, thus confirming the findings of Ref. [10] but now at lower values of W . It should be noted, however, that the data collected at $W < 4$ GeV – as displayed in Fig. 3 – show a steep rise with decreasing W that is not reproduced by the calculations of Ref. [10]. As was mentioned above, this is presumably caused by additional reaction processes that are not contained in the theoretical framework of Ref. [10]. Without explicit calculations that include these effects, it cannot be excluded that there is a finite contribution due to such processes above $W = 4$ GeV, especially at the lowest Q^2 values.

The NMC data (also shown in Fig. 5) can be compared to the calculations of Ref. [10] as well. This leads to differently normalized curves (dashed lines in Fig. 5). If the NMC normalization is adopted, the curves fall below the E665 and HERMES data. Within the constraints of the present model calculation, the E665 normalization is therefore preferred. However, on the basis of the HERMES data alone no such distinction can be made.

5.3 The longitudinal cross section

The results of recent OFPD calculations, such as those described in Refs. [5–8], only concern the longitudinal component σ_L of the ρ^0 virtual-photoproduction cross section, because the factorization theorem [3] applies only to the longitudinal case. Hence, values of σ_L were extracted from the data.

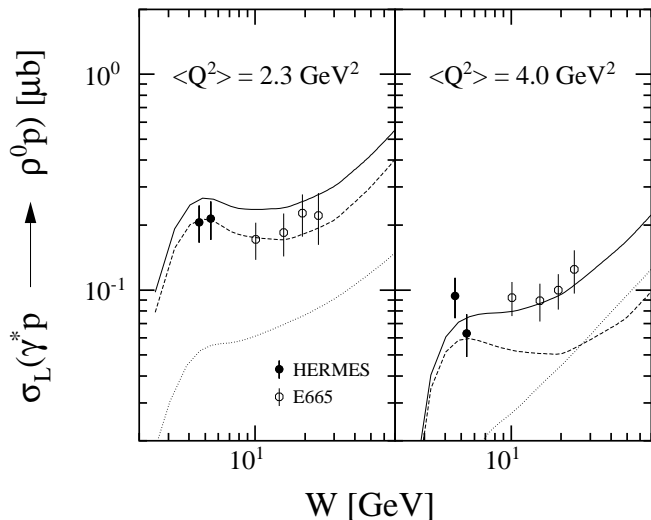


Fig. 6. The longitudinal component of the virtual-photon production cross section for ρ^0 production versus W at average Q^2 values of 2.3 (left) and 4.0 GeV^2 (right). The solid lines represent the results of the calculations of Refs. [5, 6]. The dashed (dotted) curves represent the quark (two-gluon) exchange contributions within these calculations.

The longitudinal cross section σ_L is related to the total ρ^0 production cross section $\sigma_{\gamma^*p \rightarrow \rho^0 p}$:

$$\sigma_L = \frac{R}{1 + \epsilon R} \sigma_{\gamma^*p \rightarrow \rho^0 p}. \quad (6)$$

Assuming SCHC the ratio $R = \sigma_L/\sigma_T$ can be derived from the longitudinal fraction r_{00}^{04} of ρ^0 mesons, which can be extracted from their polar decay angular distribution $W(\cos\Theta)$. In Ref. [14] such an analysis is presented, which has provided us with the parameterization of R shown in Eq. (3). This has been used to evaluate σ_L for each of the cross sections listed in Table 1. (Note that ϵ can be determined from the kinematics of each event.) The results are listed in Table 3 and, for $Q^2 > 2 \text{ GeV}^2$, displayed in Fig. 6. It may be noted that the values of σ_L increase by about 30% if the quoted parameterization of R for $W > 7 \text{ GeV}$ is used.

The data are compared to the model calculations described in Ref. [5], but with the improvements described in Ref. [6]: higher twist effects are included in a phenomenological fashion, the Q^2 -dependence of the strong coupling constant α_s was accounted for, and the sea quarks are included using the MRST98 parton distributions [37]. As can be seen from Fig. 17 of Ref. [6] the higher-twist contributions, which were included through the dependence on the intrinsic transverse momentum k_\perp , reduce the longitudinal cross section by typically a factor of 5 at $Q^2 \approx 2 \text{ GeV}^2$. As the (phenomenological) higher twist corrections at lower Q^2 values are even larger, the comparison between the OFPD calculations of Ref. [5,6] and the data has not been extended to the data below $Q^2 \approx 2 \text{ GeV}^2$. Moreover, the OFPD calculations cannot be used for data collected at $W < 4 \text{ GeV}$, as no other reaction channels were included.

Table 3. Longitudinal cross sections σ_L for ρ^0 virtual photoproduction on ^1H in μb . The listed uncertainties include both the total error on the measured ρ^0 virtual-photon production cross sections and the error on the parameterization of R for $W < 7 \text{ GeV}$, which was used in the evaluation of Eq. (6). The average values of ϵ for each bin are listed as well.

$\langle Q^2 \rangle$ [GeV^2]	$\langle W \rangle = 4.6 \text{ GeV}$ $\langle \epsilon \rangle$	$\langle W \rangle = 5.4 \text{ GeV}$ $\langle \epsilon \rangle$	σ_L [μb]	σ_L [μb]
0.83	0.87	0.74	0.77 ± 0.16	0.67 ± 0.14
1.3	0.87	0.73	0.35 ± 0.07	0.41 ± 0.08
2.3	0.86	0.71	0.21 ± 0.04	0.21 ± 0.04
4.0	0.83	0.69	0.09 ± 0.02	0.06 ± 0.01

The OFPD calculations are compared in Fig. 6 to the longitudinal cross sections measured by E665 [17] and the present experiment. The calculated contributions due to quark exchange (dashed curves) and two-gluon exchange (dotted curves) are also shown separately. In the present kinematic domain the quark contributions dominate, and only at $Q^2 = 4.0 \text{ GeV}^2$ and $W > 10 \text{ GeV}$ the gluon contribution starts to contribute significantly. A fairly good agreement between the calculations and the data is obtained, given the existing theoretical uncertainties related to the size of the higher-twist contributions, and the relatively low Q^2 values involved. The calculated rise of the cross section at $W \approx 5 \text{ GeV}$, which is associated with the contribution due to the exchange of valence quarks, is not inconsistent with the new HERMES data.

6 Summary

In summary, cross sections have been presented for exclusive diffractive ρ^0 virtual photoproduction in the W -domain between 4 and 6 GeV . The Q^2 -dependence of the cross section is well described by the propagator of the Vector Meson Dominance model, although an increase of the exponent from its original value of 2 to about 2.5 is needed when consistency with existing data for $R = \sigma_L/\sigma_T$ is required. By extrapolating the $\gamma^*p \rightarrow \rho^0 p$ cross section to $Q^2 = 0$, photoproduction cross sections are found which are in fair agreement with previously published values of about $11 \mu\text{b}$. The W -dependence of the present and (most) existing data in the W -domain between 4 and 25 GeV is well described by a model linking the x -dependence of the proton structure function $F_2^p(x, Q^2)$ to the vector meson production cross section. The longitudinal component of the cross section has been compared to calculations based on the Off-Forward Parton Distribution framework. A fairly good agreement with the data is found.

We gratefully acknowledge the DESY Directorate for its support and the DESY staff and the staffs of the collaborating institutions. We particularly appreciate the efforts of the HERA machine group in providing high beam polarization. Additional support for this work was provided by the Deutscher Akad-

emischer Austauschdienst (DAAD) and INTAS, HCM, and TMR network contributions from the European Community.

References

1. A.V. Radyushkin, Phys. Lett. B **380** (1996) 417; Phys. Rev. D **56** (1997) 5524.
2. X. Ji, Phys. Rev. Lett. **78** (1997) 610; Phys. Rev. D **55** (1997) 7114.
3. J.C. Collins, L. Frankfurt and M. Strikman, Phys. Rev. D **56** (1997) 2982.
4. L. Frankfurt, W. Koepf and M. Strikman, Phys. Rev. D **54** (1996) 3194.
5. M. Vanderhaeghen, P.A.M. Guichon and M. Guidal, Phys. Rev. Lett. **80** (1998) 5064.
6. M. Vanderhaeghen, P.A.M. Guichon and M. Guidal, Phys. Rev. D **60** (1999) 094017.
7. L. Mankiewicz, G. Piller and T. Weigl, Eur. Phys. J. C **5** (1998) 119.
8. L. Mankiewicz, G. Piller and A. Radyushkin, Eur. Phys. J. C **10** (1999) 307; and L. Mankiewicz, G. Piller and T. Weigl, Phys. Rev. D **59** (1999) 017501.
9. A.V. Belitsky, D. Müller, L. Niedermeier and A. Schäfer, hep-ph/9908337.
10. L.P.A. Haakman, A. Kaidalov and J.H. Koch, Phys. Lett. B **365** (1996) 411.
11. HERMES Collaboration, K. Ackerstaff *et al.*, Nucl. Instr. and Meth. A **417** (1998) 230.
12. J. Stewart, Proc. of the Workshop "Polarized gas targets and polarized beams," eds. R.J. Holt and M.A. Miller, Urbana-Champaign, USA, AIP Conf. Proc. 421 (1997) 69.
13. M. Kolstein, PhD Thesis, Vrije Universiteit, Amsterdam (1998), HERMES Report 98-046.
14. HERMES Collaboration, K. Ackerstaff *et al.*, submitted to Eur. Phys. J., DESY preprint 99-199 (1999), hep-ex/0002016.
15. LEPTO: G. Ingelmann, A. Edin and J. Rathsman, Comp. Phys. Comm. **101** (1997) 108.
16. M. Arneodo, L.Lamberti and M. Ryskin, DESY preprint 96-149 (1996).
17. E665 Collaboration, M.R. Adams *et al.*, Z. Phys. C **74** (1997) 237.
18. M. Ross and L. Stodolsky, Phys. Rev. **149** (1966) 1172.
19. C. Caso *et al.* (Particle Data Group), Eur. Phys. J. C **3** (1998) 1.
20. HERMES Collaboration, K. Ackerstaff *et al.*, Phys. Rev. Lett. **82** (1999) 3025.
21. NMC Collaboration, M. Arneodo *et al.*, Phys Lett. B **364** (1995) 107; NMC Collaboration, P. Amaudruz *et al.*, Phys Lett. B **295** (1992) 159.
22. H1 Collaboration, C. Adloff *et al.*, Z. Phys. C **75** (1997) 607.
23. Y. Akimov *et al.*, Phys. Rev. D **14** (1976) 3148.
24. H. Holtmann *et al.*, Z. Phys. C **69** (1996) 297.
25. I. Akushevich, Eur. Phys. J. C **8** (1999) 457; and I. Akushevich, A. Ilychev, N. Shumeiko, A. Soroko and A. Tolkachev, Comp. Phys. Comm. **104** (1997) 201.
26. P. Joos *et al.*, Nucl. Phys. B **113** (1976) 53.
27. C. del Papa *et al.*, Phys. Rev. D **19** (1979) 1303.
28. D.G. Cassel *et al.*, Phys. Rev. D **24** (1981) 2787.
29. W.D. Shambroom *et al.*, Phys. Rev. D **26** (1982) 1.
30. NMC Collaboration, M. Arneodo *et al.*, Nucl. Phys. B **429** (1994) 503.
31. ZEUS Collaboration, J. Breitweg *et al.*, Eur. Phys. J. C **6** (1999) 603.
32. T.H. Bauer *et al.*, Rev. Mod. Phys. **50** (1978) 261.
33. ZEUS Collaboration, J. Breitweg *et al.*, Eur. Phys. J. C **2** (1998) 247.
34. S.J. Brodsky *et al.*, Phys. Rev. D **50** (1994) 3134.
35. H1 Collaboration, C. Adloff *et al.*, Eur. Phys. J. **C13** (2000) 371.
36. A. Capella, A. Kaidalov, C. Merino and J. Tran Tanh Van, Phys. Lett. B **337** (1994) 358.
37. A. D. Martin, R. G. Roberts, W. J. Stirling, and R. S. Thorne (MRST 98), Eur. Phys. J. C **4** (1998) 463.